


## Band engineering and recombination mechanisms in lead-free perovskite solar cells

Wei Liu(刘维), Tingxue Zhou(周庭雪), Liang Chu(楚亮), and Xing'ao Li(李兴鳌)
**Citation:**Chin. Phys. B, 2026, 35 (**2**): 028801. DOI: 10.1088/1674-1056/ae156b
http://cpb.iphy.ac.cn; http://iopscience.iop.org/cpb

**What follows is a list of articles you may be interested in**

---

## SolarDesign: An online photovoltaic device simulation and design platform

Wei E. I. Sha(沙威), Xiaoyu Wang(王啸宇), Wenchao Chen(陈文超), Yuhao Fu(付钰豪), Lijun Zhang(张立军), Liang Tian(田亮), Minshen Lin(林敏慎), Shudi Jiao(焦书迪), Ting Xu(徐婷), Tiange Sun(孙天歌), and Dongxue Liu(刘冬雪)
Chin. Phys. B, 2025, 34 (**1**): 018801. DOI: 10.1088/1674-1056/ad9017

## Nano Ag-enhanced photoelectric conversion efficiency in all-inorganic, hole-transporting-layer-free $CsPbIBr_2$ perovskite solar cells

Youming Huang(黄友铭), Yizhi Wu(吴以治), Xiaoliang Xu(许小亮), Feifei Qin(秦飞飞), Shihan Zhang(张诗涵), Jiakai An(安嘉凯), Huijie Wang(王会杰), and Ling Liu(刘玲)
Chin. Phys. B, 2022, 31 (**12**): 128802. DOI: 10.1088/1674-1056/ac89e8

## Reveal the large open-circuit voltage deficit of all-inorganic$CsPbIBr_2$ perovskite solar cells

Ying Hu(胡颖), Jiaping Wang(王家平), Peng Zhao(赵鹏), Zhenhua Lin(林珍华), Siyu Zhang(张思玉), Jie Su(苏杰), Miao Zhang(张苗), Jincheng Zhang(张进成), Jingjing Chang(常晶晶), and Yue Hao(郝跃)
Chin. Phys. B, 2022, 31 (**3**): 038804. DOI: 10.1088/1674-1056/ac464b

## Charge transfer modification of inverted planar perovskite solar cells by $NiO_x$/Sr:$NiO_x$ bilayer hole transport layer

Qiaopeng Cui(崔翘鹏), Liang Zhao(赵亮), Xuewen Sun(孙学文), Qiannan Yao(姚倩楠), Sheng Huang(黄胜), Lei Zhu(朱磊), Yulong Zhao(赵宇龙), Jian Song(宋健), and Yinghuai Qiang(强颖怀)
Chin. Phys. B, 2022, 31 (**3**): 038801. DOI: 10.1088/1674-1056/ac1fda

## $TiO_2$/$SnO_2$ electron transport double layers with ultrathin $SnO_2$ for efficient planar perovskite solar cells

Can Li(李灿), Hongyu Xu(徐宏宇), Chongyang Zhi(郅冲阳), Zhi Wan(万志), and Zhen Li(李祯)
Chin. Phys. B, 2022, 31 (**11**): 118802. DOI: 10.1088/1674-1056/ac8349

---

# Band engineering and recombination mechanisms in lead-free perovskite solar cells

Wei Liu(刘维)[1], Tingxue Zhou(周庭雪)[1], Liang Chu(楚亮)[2,†], and Xing'ao Li(李兴鳌)[1,‡]

[1] *New Energy Technology Engineering Laboratory of Jiangsu Province & Institute of Advanced Materials & School of Science, Nanjing University of Posts and Telecommunications, Nanjing* 210023, *China*

[2] *Institute of Carbon Neutrality and New Energy & School of Electronics and Information, Hangzhou Dianzi University, Hangzhou* 310018, *China*

(Received 20 August 2025; revised manuscript received 30 September 2025; accepted manuscript online 21 October 2025)

All-inorganic lead-free perovskite solar cells have emerged as environmentally benign candidates; however, their device performance is still constrained by pronounced carrier recombination losses in the bulk and at interfaces. By combining energy band alignment analysis with detailed modeling of recombination mechanisms, a systematic strategy for optimizing hole transport layers is developed. The results reveal that a negative valence band offset produces a cliff-like interface, which facilitates hole extraction while also accounting for the observed variations in open-circuit voltage. Furthermore, short-circuit current losses are quantitatively attributed to different recombination pathways, modeled by incorporating radiative, Shockley–Read–Hall, Auger, and interface recombination processes. This comprehensive approach not only clarifies the correlation between energy level alignment and recombination dynamics but also highlights the competing roles of band offset and interface defects in determining device performance. The optimized device architecture, based on Ge-based lead-free perovskites, achieves a power conversion efficiency of 25.1%, with an open-circuit voltage of 1.29 V, a short-circuit current density of 22.5 mA·cm$^{-2}$, and a fill factor of 86.3%. These findings provide theoretical guidance for designing stable, high-performance, and environmentally friendly lead-free perovskite solar cells.

**Keywords:** perovskite solar cells, lead-free, band engineering, recombination

**PACS:** 88.40.H–, 88.40.hj

**DOI:** 10.1088/1674-1056/ae156b **CSTR:** 32038.14.CPB.ae156b

## 1. Introduction

In recent years, perovskite solar cells (PSCs) have experienced rapid development owing to their outstanding optoelectronic properties, facile low-cost fabrication processes, and compatibility with scalable deposition techniques. Their power conversion efficiencies (PCE) have approached those of conventional crystalline silicon solar cells ($> 27\%$).[1,2] The exceptional characteristics of perovskite materials, including high absorption coefficients, long carrier diffusion lengths, low exciton binding energies, and tunable bandgaps, endow them with tremendous potential for diverse next-generation photovoltaic applications.[3,4] However, non-radiative recombination remains a major bottleneck severely restricting both the efficiency and operational stability of PSCs.[5–7] This includes mechanisms such as Shockley–Read–Hall (SRH) recombination, Auger recombination, electron–phonon coupling, and tail-state-assisted recombination.[8–10] These detrimental processes not only cause significant deviations in open-circuit voltage ($V_{oc}$), short-circuit current density ($J_{sc}$), fill factor (FF), and overall device efficiency from the ideal radiative limit, but also exacerbate ion migration and chemical degradation within the absorber layer, further accelerating performance deterioration under prolonged illumination or damp heat conditions.[11,12] Therefore, the careful, deliberate, and effective regulation of non-radiative recombination processes is crucial for further enhancing PSC performance, ensuring long-term operational stability, and significantly extending overall device lifetimes and reliability.

Among various lead-free alternatives, group 14 element germanium (Ge) in its divalent state (Ge(II)) has emerged as a highly promising and environmentally friendly substitute for toxic lead in advanced perovskite materials.[13] Ge(II) shares a similar valence state with Pb(II) but possesses a lower electronegativity, offering new opportunities for rationally designing lead-free perovskite systems with improved environmental safety, long-term stability, and enhanced device performance.[14] Hu *et al.*[15] introduced Ge doping to construct vertically graded homojunction structures, effectively mitigating self-doping and high defect recombination in Sn-based perovskites, thereby substantially enhancing both film quality and device operational stability. All-inorganic $CsGeI_2Br$-based perovskites exhibit several remarkable advantages, including non-toxicity, an ideal bandgap ($\sim$1.579 eV), high absorption coefficient in the visible range ($> 10^5$ cm$^{-1}$), and excellent electrical conductivity, making them highly attractive for next-generation high-performance photovoltaic applications.[16] Compared to organic–inorganic

†Corresponding author. E-mail: chuliang@hdu.edu.cn

‡Corresponding author. E-mail: lxahbmy@126.com

© 2026 Chinese Physical Society and IOP Publishing Ltd. All rights, including for text and data mining, AI training, and similar technologies, are reserved.

hybrid perovskites, the incorporation of $Cs^+$ significantly improves both thermal and moisture stability, as confirmed by complementary experimental and theoretical studies.[17,18] In terms of device engineering, Ainane *et al.*[19] employed SCAPS-1D simulations to identify $SnO_2$ and CuI as optimal electron transport layer (ETL) and hole transport layer (HTL) materials, achieving a PCE of 15.68% for $CsGeI_3$-based devices. Similarly, Sarkar *et al.*[20] constructed a $TiO_2$/$CsGeI_2Br$/Spiro-OMeTAD device model using SCAPS-1D and achieved a theoretical PCE of up to 25.15% by carefully tuning energy band alignment, interface matching, and carrier transport properties. These findings highlight the substantial potential of Ge-based perovskite materials in advanced next-generation photovoltaic applications and offer valuable theoretical insights for further device structure optimization, precise interface engineering, and process refinement.

In this study, a comprehensive series of lead-free PSCs were modeled using the SCAPS-1D simulation platform tool, employing $CsGeI_2Br$ as the primary light-absorbing layer, with $CsSnI_3$, $CsGeI_3$, $CsSn_{0.5}Ge_{0.5}I_3$, and $CsGeI_2Br$ itself serving as HTLs. Energy band alignment analysis, in conjunction with detailed recombination mechanism modeling, was employed to systematically screen and optimize the HTL. Particular attention was given to the impact of non-radiative recombination processes, including intrinsic defect-assisted recombination and interface recombination, on overall device performance. By systematically tuning material parameters, band alignment, and recombination pathways, this work proposes effective strategies for improving photovoltaic efficiency, suppressing performance degradation, and extending operational stability. These findings provide valuable theoretical insights and practical guidance for the rational design and development of stable, high-performance, and environmentally friendly lead-free PSCs.

## 2. Calculation methods

The simulation is carried out using the widely adopted solar cell capacitance simulator, SCAPS-1D (one-dimensional solar cell simulation program).[21] The AM1.5G standard solar spectrum was employed with an illumination intensity set to 1000 $W{\cdot}m^{-2}$ to ensure consistent, reproducible, and comparable light conditions, while the ambient temperature was carefully maintained at 300 K. All efficiency data reported in this work were obtained directly from SCAPS-1D simulations. The simulated device architecture was based on a typical n–i–p configuration, comprising fluorine-doped tin oxide glass (FTO), an ETL, a perovskite absorber layer, an HTL, and a back electrode. Four lead-free perovskite materials ($CsSnI_3$, $CsGeI_3$, $CsSn_{0.5}Ge_{0.5}I_3$, and $CsGeI_2Br$) were systematically investigated as potential HTL candidates, with $WS_2$ employed as the ETL. In the interband recombination model, the recombination rates at the FTO, ETL, and HTL were set to zero, while the radiative recombination coefficient ($3 \times 10^{-11}$ $cm^3{\cdot}s^{-1}$) and Auger recombination coefficient ($1 \times 10^{-29}$ $cm^6{\cdot}s^{-1}$) were consistently kept constant. Key simulation parameters for the HTL, ETL, and $CsGeI_2Br$ absorber layer are summarized in Table 1, and the interface defect parameters between the transport layers and the $CsGeI_2Br$ absorber are detailed in Table 2. The parameters listed in Table 1 represent the fundamental physical quantities employed in the SCAPS-1D simulations. Specifically, $d$ denotes the precise layer thickness, while $E_g$ and $\chi$ correspond to the bandgap and electron affinity, respectively. The relative dielectric permittivity is given by $\varepsilon_r$. The effective densities of states in the conduction and valence bands are represented by $N_c$ and $N_v$. Carrier transport characteristics are comprehensively described by the electron and hole thermal velocities ($V_e$ and $V_h$) as well as the corresponding mobilities ($\mu_n$ for electrons and $\mu_p$ for holes). In addition, $N_D$ and $N_A$ indicate the donor and acceptor densities, respectively, whereas $N_t$ accounts for the intrinsic defect density.

**Table 1.** Physical parameters of different layers in PSCs.

| Parameter | FTO[17] | n-$WS_2$[18] | i-$CsGeI_2Br$[19] | p-$CsGeI_2Br$[19] | p-$CsSnI_3$[16] | p-$CsGeI_3$[22] | p-$CsSn_{0.5}Ge_{0.5}I_3$[13] |
|---|---|---|---|---|---|---|---|
| $d$ (nm) | 500 | 100 | 600 | 300 | 300 | 300 | 300 |
| $E_g$ (eV) | 3.5 | 1.8 | 1.67[22] | 1.67 | 1.3 | 1.63[13] | 1.5 |
| $\chi$ (eV) | 4.0 | 3.95 | 3.76 | 3.76 | 3.62 | 3.45[23] | 3.9 |
| $\varepsilon_r$ | 9.0 | 13.6 | 5.85 | 5.85 | 48.2 | 18.6[24] | 28 |
| $N_c$ ($cm^{-3}$) | $2.2 \times 10^{18}$ | $1 \times 10^{19}$ | $9.65 \times 10^{17}$ | $9.65 \times 10^{17}$ | $1.57 \times 10^{19}$ | $1.0 \times 10^{18}$ | $3.1 \times 10^{18}$ |
| $N_v$ ($cm^{-3}$) | $1.8 \times 10^{19}$ | $2.4 \times 10^{19}$ | $1.04 \times 10^{18}$ | $1.04 \times 10^{18}$ | $1.47 \times 10^{18}$ | $1.0 \times 10^{19}$ | $3.1 \times 10^{18}$ |
| $V_h$ ($cm{\cdot}s^{-1}$) | $1 \times 10^7$ | $1 \times 10^7$ | $1 \times 10^7$ | $1 \times 10^7$ | $1 \times 10^7$ | $1 \times 10^7$ | $1 \times 10^7$ |
| $V_e$ ($cm{\cdot}s^{-1}$) | $1 \times 10^7$ | $1 \times 10^7$ | $1 \times 10^7$ | $1 \times 10^7$ | $1 \times 10^7$ | $1 \times 10^7$ | $1 \times 10^7$ |
| $\mu_n$ ($cm^2{\cdot}V^{-1}{\cdot}s^{-1}$) | 20 | 100 | 20 | 20 | 50 | 20 | 974 |
| $\mu_p$ ($cm^2{\cdot}V^{-1}{\cdot}s^{-1}$) | 10 | 100 | 20 | 20 | 400 | 20 | 213 |
| $N_D$ ($cm^{-3}$) | $1.8 \times 10^{19}$ | $1 \times 10^{18}$ | 0 | 0 | 0 | 0 | 0 |
| $N_A$ ($cm^{-3}$) | 0 | 0 | $2 \times 10^{16}$ | $2 \times 10^{16}$ | $5 \times 10^{17}$ | $2 \times 10^{16}$ | $1 \times 10^{14}$ |
| $N_t$ ($cm^{-3}$) | $1 \times 10^{15}$ | $1 \times 10^{15}$ | $1 \times 10^{16}$ | $1 \times 10^{15}$ | $1 \times 10^{15}$ | $1 \times 10^{15}$ | $1 \times 10^{15}$ |

**Table 2.** Simulation parameters for interfacial defects at the CsGeI2Br/HTLs.

| Interface | Defect type | Capture cross section: electrons/holes ($cm^2$) | Energetic distribution | Reference for defect energy level | Total density ($cm^{-3}$) |
|---|---|---|---|---|---|
| ETL/$CsGeI_2Br$ | neutral | $1\times10^{-19}/1\times10^{-19}$ | single | above the VBM | $1\times10^{10}$ |
| $CsGeI_2Br$/HTL | neutral | $1\times10^{-19}/1\times10^{-19}$ | single | above the VBM | $1\times10^{10}$ |

## 3. Results and discussion

### 3.1. Basic photovoltaic performance of the device

To evaluate the fundamental performance of the devices, an n-i-p structured model was constructed as follows: it consists of an FTO substrate, a 100 nm thick $WS_2$ electron transport layer, a $CsGeI_2Br$ perovskite absorber layer with an initial thickness of 600 nm, HTLs including $CsSnI_3$, $CsGeI_3$, $CsSn_{0.5}Ge_{0.5}I_3$, and $CsGeI_2Br$ (each 300 nm thick), and a metal back electrode. The initial defect density of the perovskite layer was set to $1\times10^{15}$ $cm^{-3}$, with electron and hole mobilities both at 20 $cm^2\cdot V^{-1}\cdot s^{-1}$, and an Auger recombination coefficient of $1\times10^{-29}$ $cm^6\cdot s^{-1}$.[22] Under standard AM1.5G illumination, as shown in Figs. 1(a)–1(d), the device employing $CsGeI_3$ as the HTL exhibited the optimal *J*–*V* characteristics.

Furthermore, the comparison of $V_{oc}$, $J_{sc}$, FF, and PCE in Fig. 1(e) clearly indicates that the $CsGeI_3$-based system outperforms the others, with a $V_{oc}$ of 1.29 V, an FF of 86.34%, and a PCE of 25.06%. As further mechanistic analysis in

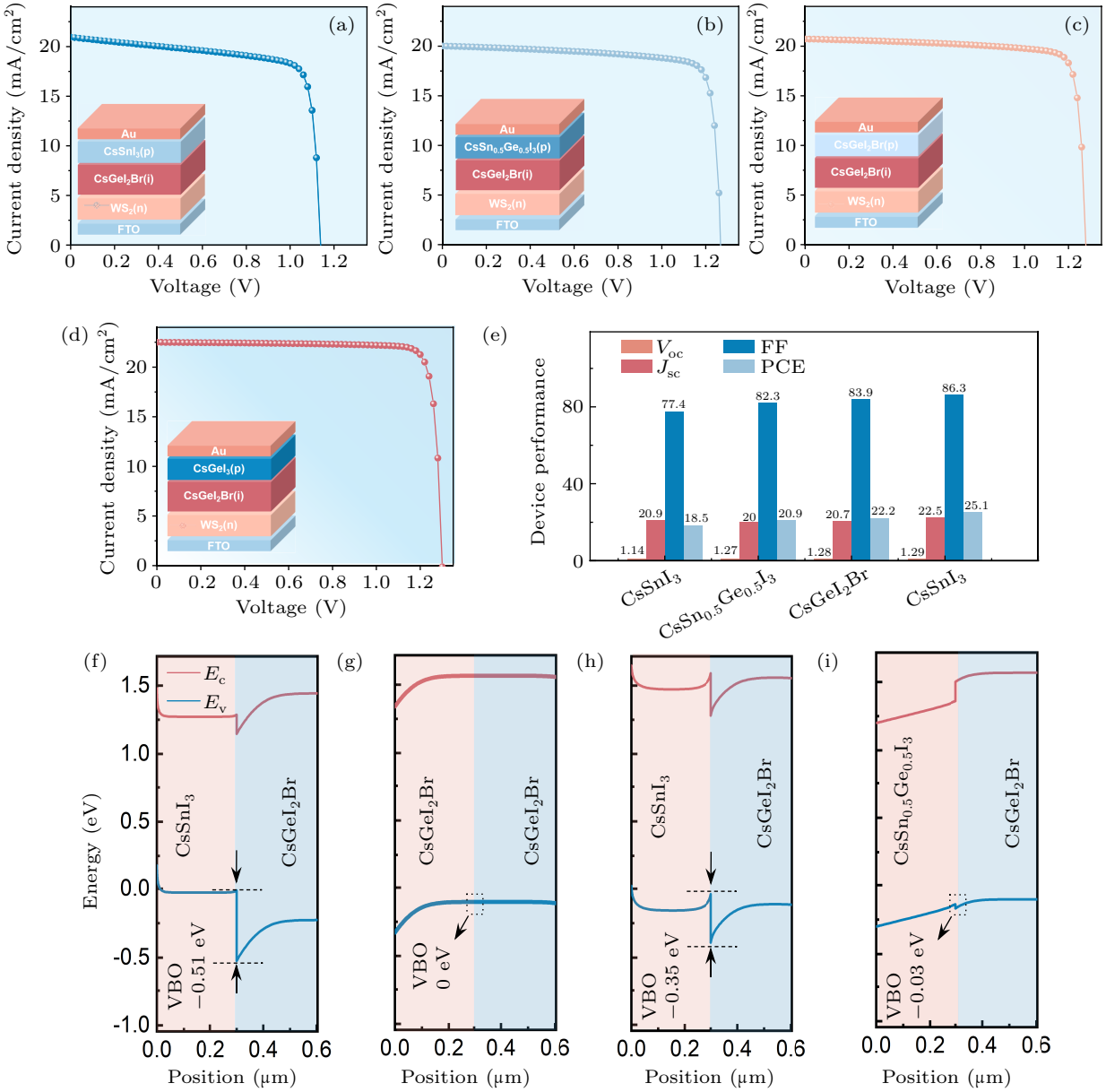



**Fig. 1.** *J*–*V* characteristics of devices with four different HTL configurations: (a) $CsSnI_3$, (b) $CsSn_{0.5}Ge_{0.5}I_3$, (c) $CsGeI_2Br$, and (d) $CsGeI_3$. (e) Comparison of photovoltaic performance parameters. (f)–(i) Energy band diagrams at the $CsGeI_2Br$/HTL interface for devices with the four respective HTL configurations.

Fig. 1(f) reveals, this performance advantage originates from improved band alignment and a reduced interface recombination rate between $CsGeI_3$ and the absorber layer. The intrinsic mechanisms underlying the superior performance of $CsGeI_3$ as an HTL can thus be elucidated through interface band engineering and carrier dynamics analysis. The device employing $CsGeI_3$ as the HTL exhibits the optimal *J*–*V* characteristics, with a $J_{sc}$ reaching 22.49 mA·cm$^{-2}$, which is significantly higher than those of the other three configurations. This advantage is particularly evident in the external quantum efficiency (EQE) response within the 500–600 nm wavelength range (Fig. 2(a)), indicating superior carrier collection efficiency for $CsGeI_3$. As shown in Fig. 2(b), the short-circuit current density ($J_{sc}$) exhibits significant variations under the four different HTL configurations. Specifically, devices with $CsSn_{0.5}Ge_{0.5}I_3$ and $CsGeI_2Br$ as HTLs display relatively lower $J_{sc}$, whereas those with $CsSnI_3$ and $CsGeI_3$ exhibit markedly enhanced $J_{sc}$, with the $CsGeI_3$-based device achieving the highest value. These results indicate that the energy-level alignment and interfacial properties of the HTL play a crucial role in the efficient collection and transport of photogenerated carriers. To further elucidate the origin of the $J_{sc}$ differences, Fig. 2(c) schematically illustrates the $J_{sc}$ loss mechanisms, which primarily include current leakage associated with shunt resistance ($J_{shunt}$) and interface/bulk recombination losses ($J_{Re}$). Quantitative analysis in Fig. 2(d) reveals that the $J_{Re}$ of the $CsSn_{0.5}Ge_{0.5}I_3$ and $CsGeI_2Br$ systems is relatively high, indicating more severe interfacial recombination that limits the effective current output. In contrast, the $CsGeI_3$-based device exhibits a significantly lower $J_{Re}$, suggesting superior interfacial compatibility and carrier transport capability, which accounts for its highest $J_{sc}$. Meanwhile, $J_{shunt}$ losses for all devices remain at low levels, indicating that the influence of shunt resistance on $J_{sc}$ is relatively minor.

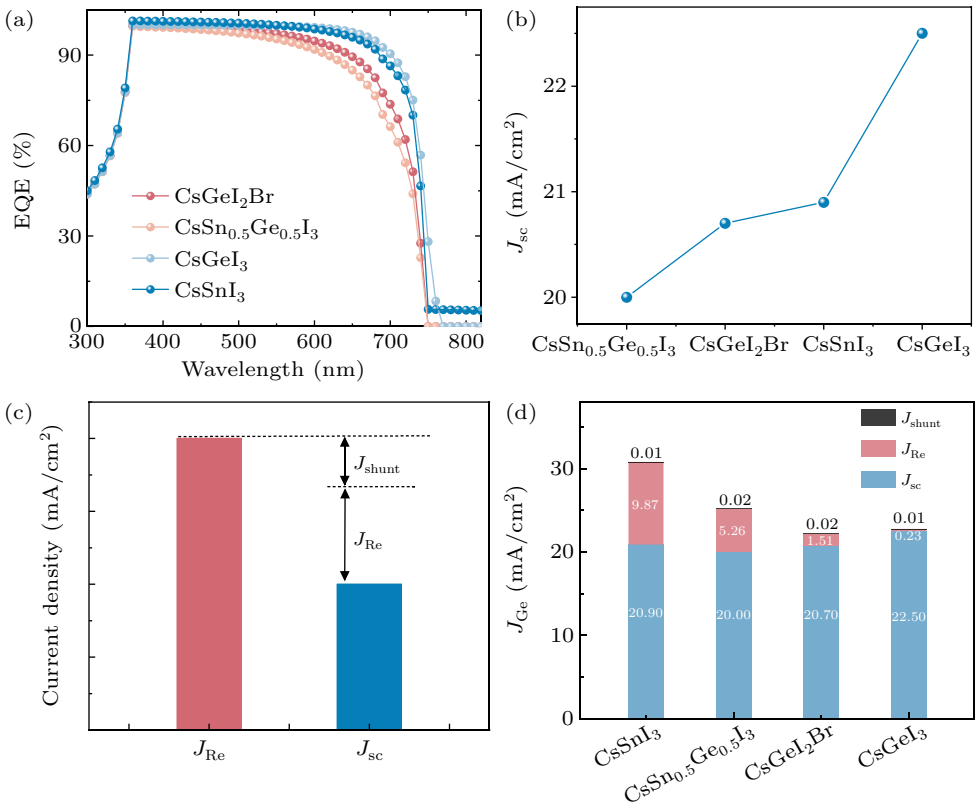



**Fig. 2.** Device characteristics under four different HTL configurations: (a) EQE spectra. (b) Comparison of $J_{sc}$ for the four device structures. (c) Schematic illustration of the $J_{sc}$ loss mechanisms. (d) Quantitative analysis of $J_{sc}$ loss for the four device configurations.

Prior to conducting in-depth analyses, a systematic investigation of the $J_{sc}$ loss mechanisms is essential. Such an analysis not only facilitates a comprehensive understanding of the underlying physical processes governing device performance optimization but also provides theoretical insights into the key factors influencing PCE. Therefore, a comprehensive investigation combining energy level alignment and systematic $J_{sc}$ loss analysis was conducted to elucidate the underlying reasons for the differing photovoltaic performances among various transport layers. In this study, the loss mechanisms affecting $J_{sc}$ were thoroughly examined (Fig. 2(c)), with the corresponding theoretical model expressed by the following equation:[16]

$$J_{sc} = J_{Ge} - J_{Re} - J_{shunt}, \tag{1}$$

$$J_{sc} = J_{Ge} - J_0\left(e^{\frac{q(V+J_{sc}R_s)}{n_{id}kT}} - 1\right) - \frac{(V+J_{sc}R_s)}{R_{sh}}, \tag{2}$$

where $J_{Ge}$ denotes the photogenerated current density, $J_{shunt}$ represents the shunt current, and $J_{Re}$ corresponds to the recombination current (including both radiative and non-radiative recombination). Additional parameters include the reverse saturation current density $J_0$, diode ideality factor $n_{id}$, Boltzmann constant $k$ ($1.38 \times 10^{-23}$ J·K$^{-1}$), ambient temperature $T$, series resistance $R_s$, and shunt resistance $R_{sh}$.

To further investigate the origin of the $J_{sc}$ differences, we analyzed the energy band diagrams. As shown in Figs. 1(f)–1(i), the valence band offsets (VBOs) between the four candidate HTL materials and the perovskite absorber layer are as follows: $CsSnI_3$ (−0.51 eV), $CsSn_{0.5}Ge_{0.5}I_3$ (−0.03 eV), $CsGeI_2Br$ (0 eV), and $CsGeI_3$ (−0.35 eV). According to band alignment theory, a negative VBO (as seen in $CsSnI_3$, $CsSn_{0.5}Ge_{0.5}I_3$, and $CsGeI_3$) creates a "cliff-like" band structure at the interface, which facilitates hole extraction. However, the excessively large negative VBO of $CsSnI_3$ (−0.51 eV) leads to significant carrier accumulation at the interface, resulting in a high recombination current density ($J_{Re}$) of 9.87 mA·cm$^{-2}$ (Fig. 2(d)) and a reduced device efficiency of 18.45%. In the case of $CsSn_{0.5}Ge_{0.5}I_3$, despite having the smallest absolute VBO (−0.03 eV), its conduction band minimum (CBM = −3.90 eV) lies below that of the perovskite layer (CBM = −3.76 eV), forming a reverse electron transport barrier. This not only fails to effectively block electron diffusion toward the HTL but also causes hole trapping and recombination within the transport layer ($J_{Re} = 5.26$ mA·cm$^{-2}$), lowering the efficiency to 20.88% (Fig. 2(d)).

For $CsGeI_2Br$, the flat band alignment (VBO = 0 eV) eliminates the potential barrier but sacrifices selective carrier transport, leading to increased electron–hole recombination and a moderate efficiency of 22.19%. In contrast, $CsGeI_3$, with a moderate VBO of −0.35 eV, forms a graded band structure that ensures efficient hole extraction, supported by its high hole mobility (20 cm$^2$·V$^{-1}$·s$^{-1}$). As shown in Fig. 1(g), among the four HTL configurations, $CsGeI_3$-based devices exhibit the highest $J_{sc}$ of 22.09 mA·cm$^{-2}$, reflecting superior photogenerated carrier collection and transport, and achieve the best PCE of 25.06%. Despite these promising results, the $V_{oc}$ still shows a notable deficit compared to the Shockley–Queisser theoretical limit (1.33 V), mainly due to bulk perovskite defects (dominated by SRH recombination) and non-radiative recombination induced by energy level mismatches at the ETL/perovskite and perovskite/HTL interfaces. These findings indicate that while the initial device architecture exhibits basic photovoltaic functionality, its efficiency and stability remain far from the theoretical potential of lead-free perovskite materials. Addressing key issues such as recombination losses and band misalignment through systematic numerical optimization is therefore essential.

### 3.2. Radiative recombination in devices

In perovskite solar cells, radiative recombination is a fundamental physical process governing carrier recombination. Typically, the radiative recombination coefficient exhibits a degree of stability and does not vary significantly with different fabrication techniques. This suggests that the radiative recombination coefficient is more likely an intrinsic material property rather than a parameter influenced by processing conditions.[23] Radiative recombination is one of the fundamental carrier recombination mechanisms in semiconductor materials. It involves the direct transition of an electron from the conduction band to the valence band, where it recombines with a hole, with the recombination energy released in the form of a photon. This process can be expressed as[24]

$$U_{radiative} = K(np - n_i^2), \tag{3}$$

where $n$ and $p$ are the concentrations of electrons and holes, respectively, and $n_i$ is the intrinsic carrier concentration. Radiative recombination adheres to both energy and momentum conservation laws and serves as a fundamental mechanism enabling photon-to-electron conversion in optoelectronic devices such as solar cells. However, it also represents a key limiting factor for improving device efficiency.

Based on theoretical and experimental values of the radiative recombination coefficient for perovskites reported in the literature,[25,26] we systematically investigated the effect of radiative recombination coefficients ranging from $10^{-12}$ cm$^3$·s$^{-1}$ to $10^{-8}$ cm$^3$·s$^{-1}$ on the photovoltaic performance of four different device configurations. As shown in Fig. 3(d), when the radiative recombination coefficient gradually increases from $10^{-12}$ cm$^3$·s$^{-1}$ to $10^{-8}$ cm$^3$·s$^{-1}$, the $V_{oc}$ remains nearly constant until the coefficient reaches $10^{-8}$ cm$^3$·s$^{-1}$, where it drops abruptly. Meanwhile, the $J_{sc}$ (Fig. 3(a)) remains almost unchanged, indicating that the photogenerated current is relatively insensitive to the strength of radiative recombination. The FF shows a nonlinear dependence on the radiative recombination coefficient (Fig. 3(g)). It remains relatively high (88.18%–77.62%) when the coefficient lies in the range of $10^{-12}$–$10^{-10}$ cm$^3$·s$^{-1}$, but once this value exceeds $10^{-9}$ cm$^3$·s$^{-1}$, the FF declines significantly, dropping to 84.70%–76.63%. This trend can be attributed to the spatial redistribution of carrier concentrations induced by radiative recombination.

At lower radiative recombination coefficient values, the carrier diffusion length is sufficient to maintain a uniform concentration gradient, ensuring efficient charge extraction. In contrast, at higher radiative recombination coefficient values, rapid recombination at the transport layer interface leads to the formation of a space-charge region, thereby intensifying ohmic losses during carrier transport.[27,28] Consequently, a

pronounced negative correlation is observed between the PCE and the radiative recombination coefficient. This behavior arises from the intrinsic energy dissipation associated with radiative recombination. When sunlight is absorbed by the perovskite active layer, photon energy excites electronic transitions, generating electron–hole pairs with the potential to produce electrical energy. However, a high radiative recombination coefficient implies that carriers are more likely to recombine radiatively, re-emitting the stored energy as photons rather than contributing to electrical output. Therefore, minimizing the radiative recombination coefficient is critical to maximizing the PCE of perovskite solar cells.

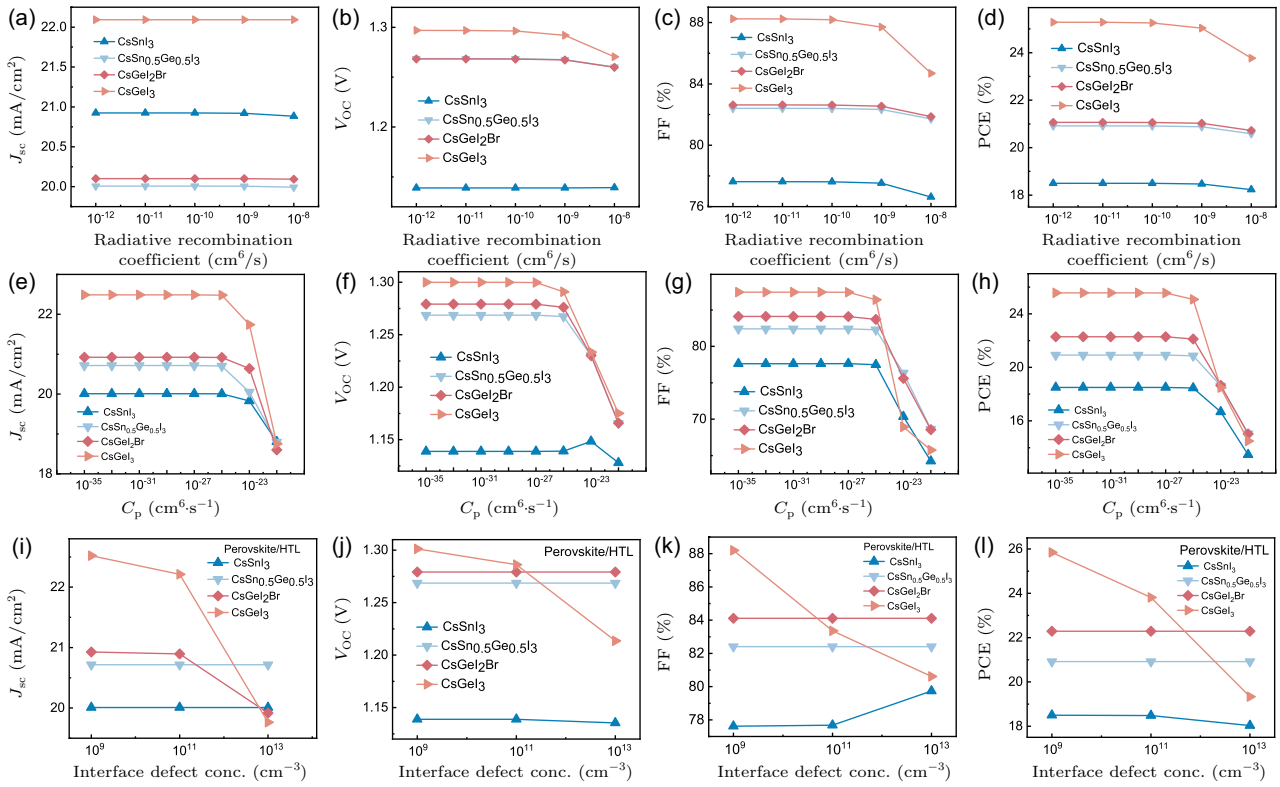



**Fig. 3.** Effects of the radiative recombination coefficient on (a) $J_{sc}$, (b) $V_{oc}$, (c) FF, and (d) PCE. Optoelectronic performance under varying Auger recombination coefficients (e)–(h). Optoelectronic performance under different interface defect conditions (i)–(l).

### 3.3. Auger recombination in devices

As a critical non-radiative recombination mechanism in perovskite solar cells, Auger recombination exerts a systematic influence on carrier dynamics throughout the processes of photogenerated carrier generation, separation, and transport.[29,30] Ultimately, it significantly limits device PCE and operational stability by reducing key parameters such as $V_{oc}$, $J_{sc}$, and FF. Figures 3(b), 3(e), 3(h), and 3(k) systematically illustrate the evolution of device performance parameters for four different HTL architectures as a function of the Auger recombination coefficient varying from $10^{-35}$ cm$^6$·s$^{-1}$ to $10^{-21}$ cm$^6$·s$^{-1}$.

In this simulation study, a baseline model was established by adopting standard Auger recombination coefficients, with both the electron ($C_n$) and hole ($C_p$) coefficients set to $1 \times 10^{-39}$ cm$^6$·s$^{-1}$. Subsequently, the quantitative impact of Auger recombination was investigated using a controlled variable approach. In our calculations, the electron and hole Auger coefficients were assumed to be equal ($C_n = C_p$). As the hole Auger recombination coefficient ($C_p$) increases from $10^{-35}$ cm$^6$·s$^{-1}$ to $10^{-21}$ cm$^6$·s$^{-1}$, all devices with the four different HTL structures exhibit systematic performance degradation, indicating that Auger recombination plays a dominant role in non-radiative carrier losses.[31,32] Notably, the extent of performance degradation varies significantly among the HTL configurations, following the order: $CsGeI_3 > CsGeI_2Br > CsSn_{0.5}Ge_{0.5}I_3 > CsSnI_3$. The device based on $CsGeI_3$ experiences the most severe efficiency drop of 43.4%, whereas the $CsSnI_3$-based device exhibits only a 17.2% reduction. It is worth noting that previous studies have reported that the typical range of $C_p$ values for perovskites lies between $10^{-30}$ cm$^6$·s$^{-1}$ and $10^{-28}$ cm$^6$·s$^{-1}$. When $C_p$ dramatically increases to $10^{-21}$ cm$^6$·s$^{-1}$, the PCEs of perovskite solar cells further decline to 13.48% ($CsSnI_3$), 15.05% ($CsSn_{0.5}Ge_{0.5}I_3$), 15.02% ($CsGeI_2Br$), and 14.49% ($CsGeI_3$). Detailed photovoltaic performance metrics are summarized in Tables S1–S4. The Auger recombination process ultimately imposes a fundamental limitation on the detailed balance performance of PSCs. Through simulation analyses incorporating both radiative and Auger recombination mechanisms, relevant studies have successfully elucidated the practical detailed balance

limits of PSCs.

### 3.4. Interface recombination in devices

The presence of interface defect densities plays a critical role in determining device stability and efficiency by impeding charge transport. To simulate realistic conditions, interface defect densities ($N_{ti}$) were introduced in the initial simulations, encompassing all relevant interfaces within the PSCs.[32] These interfaces include the HTL/$CsGeI_2Br$ and $CsGeI_2Br$/ETL interfaces. By systematically varying $N_{ti}$ at each interface, their respective impacts on PSC performance were investigated.

First, the influence of $N_{ti}$ at the HTL/$CsGeI_2Br$ interface was studied by varying its value from $10^9$ $cm^{-3}$ to $10^{13}$ $cm^{-3}$. Figures 3(c), 3(f), 3(i), and 3(l) illustrate the effects of $N_{ti}$ at the HTL/$CsGeI_2Br$ interface on PSC characteristics. As $N_{ti}$ increases from $10^9$ $cm^{-3}$ to $10^{13}$ $cm^{-3}$, the device based on $CsSnI_3$ exhibits a slight decrease in $V_{oc}$ from 1.139 V to 1.136 V, a reduction in $J_{sc}$ from 20.92 mA/$cm^2$ to 19.92 mA/$cm^2$, an increase in FF from 77.42% to 79.62%, and a drop in PCE from 18.45% to 18.01%. Similarly, for the $CsGeI_3$-based device, $V_{oc}$ decreases from 1.30 V to 1.21 V, $J_{sc}$ declines from 22.49 mA·$cm^{-2}$ to 19.76 mA·$cm^{-2}$, FF drops from 86.85% to 80.52%, and PCE significantly decreases from 25.26% to 19.31%. Detailed photovoltaic performance metrics are summarized in Tables S5–S8.

This performance degradation originates from three primary physical mechanisms. First, a high defect density ($N_{ti} \geq 10^{12}$ $cm^{-3}$) significantly enhances recombination, with the recombination rate positively correlated with $N_{ti}$, as described by the following equation:[33]

$$U = \frac{\sigma_n \sigma_p \upsilon_{th} N_{ti}(pn - n_i^2)}{\sigma_n(n + n_i) + \sigma_p(p + n_i)}. \tag{4}$$

When $N_{ti} = 10^{13}$ $cm^{-3}$, the recombination rate increases by approximately four orders of magnitude compared with the baseline value at $N_{ti} = 10^9$ $cm^{-3}$. Second, defect states act as carrier scattering centers, leading to a reduction in carrier mobility. Third, an increased total density of interface defects exacerbates band bending at the interface, hindering carrier extraction efficiency and resulting in an overall decline in device performance. These findings are consistent with previous reports on other perovskite systems.[34]

The simulation results in Fig. S1 demonstrate that devices with the four different HTL configurations exhibit a systematic decline in $V_{oc}$, $J_{sc}$, FF, and PCE as the defect density at the $CsGeI_2Br$/ETL interface increases from $10^9$ $cm^{-3}$ to $10^{13}$ $cm^{-3}$. From a carrier dynamics perspective, interface defects act as efficient non-radiative recombination centers, significantly accelerating the SRH recombination process and causing substantial losses of photogenerated carriers. Particularly at high defect densities, the carrier capture and recombination rates far exceed the charge extraction rate, severely limiting device performance. Therefore, reducing defect densities at the $CsGeI_2Br$/HTL and ETL/$CsGeI_2Br$ interfaces is a critical optimization strategy for suppressing non-radiative recombination losses and enhancing energy conversion efficiency.[35] Experimental studies have confirmed that interface passivation treatments can effectively reduce defect densities to below $10^{10}$ $cm^{-3}$, significantly prolonging carrier lifetimes and substantially improving device performance.[36]

### 3.5. SRH recombination in devices

SRH recombination is recognized as one of the primary mechanisms limiting PSC performance.[37] The SRH recombination rate is strongly influenced by both the bulk defect density of the material and the energy level position of the defects. Based on their relative positions within the bandgap, defects are typically categorized into shallow levels (0–0.15 eV and 1.75–1.90 eV), quasi-deep levels (0.16–0.45 eV and 1.45–1.75 eV), and deep levels (0.45–1.44 eV). The analysis focuses on two representative defect levels, 0.1 eV (shallow) and 0.6 eV (deep), to assess their respective impacts on device performance. A systematic analysis was conducted to investigate the influence of these defects on the optoelectronic performance of four device architectures, with defect densities ranging from $10^{13}$ $cm^{-3}$ to $10^{16}$ $cm^{-3}$. As shown in Fig. S2, when the shallow defect density remains below $10^{15}$ $cm^{-3}$, the device exhibits relatively stable performance in terms of $V_{oc}$, $J_{sc}$, FF, and PCE, with only minor fluctuations observed. However, as the defect density increases to $10^{16}$ $cm^{-3}$, all performance metrics begin to decline significantly, particularly FF and PCE. Taking the $CsGeI_3$-based device as an example, its FF decreases from 87.63% to 84.95%, while the PCE declines from 25.65% to 24.47%. This trend is closely correlated with the recombination rate variations shown in Fig. 4(g). The SRH recombination rate induced by shallow-level defects increases rapidly with rising defect density, resulting in shorter carrier lifetimes and enhanced recombination losses, thereby deteriorating device performance.

In contrast, deep-level defects exert a more pronounced detrimental effect on device performance.[38] As illustrated in Figs. 4(b), 4(d), 4(f), and 4(h), when the 0.6 eV deep-level defect density increases from $10^{13}$ $cm^{-3}$ to $10^{16}$ $cm^{-3}$, the recombination rate rises by approximately one order of magnitude, significantly higher than that induced by shallow defects. Specifically, when the defect density exceeds $10^{15}$ $cm^{-3}$, all four devices exhibit an FF reduction exceeding 4%. For the $CsGeI_3$-based device, the FF drops sharply by 13.9% (from 87.60% to 75.58%), and the corresponding PCE experiences a substantial decrease of 23% (from 25.63% to 19.80%). These results further confirm that deep-level defects exert a far more destructive impact on device performance than shallow-level defects.[39,40]

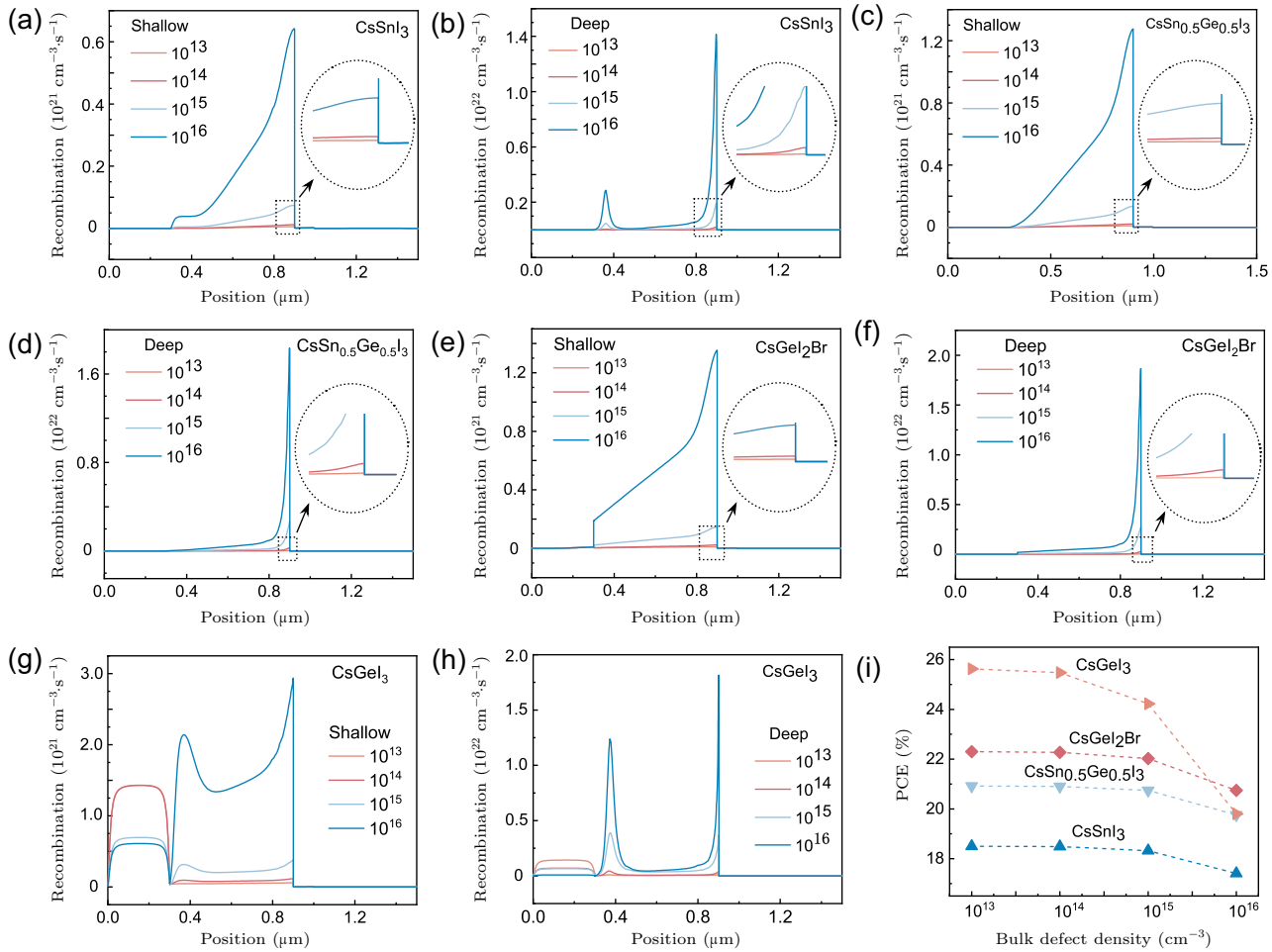



**Fig. 4.** Variation of recombination rates under shallow (0.1 eV) and deep (0.6 eV) defect levels for devices with four different HTL configurations: (a) and (b) $CsSnI_3$, (c) and (d) $CsSn_{0.5}Ge_{0.5}I_3$, (e) and (f) $CsGeI_2Br$, and (g) and (h) $CsGeI_3$. The bulk defect density ranges from $10^{13}$ cm$^{-3}$ to $10^{16}$ cm$^{-3}$. (i) Effect of deep-level bulk defects on device efficiency.

Combined with the spatial distribution analysis in Fig. 4, it is evident that defect-dominated recombination exhibits distinct spatial characteristics: recombination induced by shallow-level defects primarily occurs within the bulk region, whereas recombination caused by deep-level defects is more pronounced in both the bulk and interface regions (Figs. 4(b), 4(d), 4(f), and 4(h)). The latter, being proximal to carrier transport pathways, imposes a stronger barrier to charge extraction, thereby significantly degrading overall device performance. Moreover, as observed in Figs. S2 and S3, device performance declines sharply once the recombination rate exceeds a critical threshold of approximately $10^{15}$ cm$^{-3}$, providing a clear guideline for subsequent device design and defect management.[41]

The SRH recombination rate $R_{\mathrm{SRH}}$ quantitatively describes the number of recombination events per unit volume per unit time and is expressed as[37]

$$R_{\mathrm{SRH}} = \frac{np - n_{\mathrm{i}}^2}{(n+n_1)\tau_{\mathrm{p}} + (p+p_1)\tau_{\mathrm{n}}}, \tag{5}$$

where

$$p_1 = N_{\mathrm{V}} \exp\left(\frac{E_{\mathrm{V}} - E_{\mathrm{T}}}{kT}\right), \quad n_1 = N_{\mathrm{C}} \exp\left(\frac{E_{\mathrm{T}} - E_{\mathrm{C}}}{kT}\right),$$

and $\tau_{\mathrm{n}}$ and $\tau_{\mathrm{p}}$ denote the electron and hole lifetimes, respectively. Here, $n$ and $p$ are the electron and hole concentrations, $N_{\mathrm{C}}$ and $N_{\mathrm{V}}$ are the effective density of states in the conduction and valence bands, $E_{\mathrm{T}}$ is the trap (defect) energy level, and $E_{\mathrm{C}}$ and $E_{\mathrm{V}}$ are the conduction band minimum and valence band maximum, respectively.

In summary, while shallow-level defects can degrade performance at high defect densities, the impact of deep-level defects is substantially more severe, particularly due to their strong recombination effects at interfaces. Therefore, enhancing device stability and efficiency critically depends on preferential suppression of deep-level defect formation, with stringent control of their density below $10^{15}$ cm$^{-3}$ at interfaces to minimize non-radiative recombination losses and ensure efficient photovoltaic performance.

## 4. Conclusion and perspectives

This work demonstrates that effective suppression of non-radiative recombination, particularly SRH and interface recombination, is essential for improving the efficiency of lead-free perovskite solar cells. Through detailed SCAPS-1D nu-

merical simulations, Ge-based perovskite materials such as $CsGeI_2Br$ and $CsGeI_3$ were shown to possess promising optoelectronic properties, including suitable bandgaps, strong absorption in the visible spectrum, and enhanced intrinsic stability. Among the configurations studied, an optimal PCE of 25.1% was achieved, underscoring the potential of Ge(II) as a viable and sustainable alternative to toxic Pb(II) in perovskite absorber layers.

In addition to high efficiency, the simulations revealed that these Ge-based materials exhibit improved tolerance to defect states, particularly under reduced SRH recombination rates and optimized interface conditions. This highlights the importance of interface engineering and defect passivation in device design. The insights gained from this study provide valuable theoretical guidance for the development of next-generation, high-performance perovskite solar cells that are not only efficient and stable, but also environmentally benign.

## Acknowledgments

This project was supported by the National Natural Science Foundation of China (Grant Nos. 52102165 and 62474056) and the Natural Science Foundation of Nanjing University of Posts and Telecommunications (Grant Nos. NY221029 and NY222165).

## References

[1] *National Renewable Energy Labs (NREL), Best Research Cell Efficiencies Chart*
[2] Chung I, Lee B, He J, Chang R P H and Kanatzidis M G 2012 *Nature* **485** 486
[3] Singh S, Laxmi and Kabra D 2020 *J. Phys. D: Appl. Phys.* **53** 503003
[4] Li J, Wang H, Chin X Y, Dewi H A, Vergeer K, Goh T W, Lim J M, Lew J H, Loh K P, Soci C, Sum T C, Bolink H J, Mathews N, Mhaisalkar S and Bruno A 2020 *Joule* **4** 1035
[5] Chen J and Park N G 2019 *Adv. Mater.* **31** 1803019
[6] Liu Y, Akin S, Pan L, Uchida R, Arora N, Milic J V, Hinderhofer A, Schreiber F, Uhl A R, Zakeeruddin S M, Hagfeldt A, Dar M I and Gratzel M 2019 *Sci. Adv.* **5** eaaw2543
[7] Aydin E, De Bastiani M and De Wolf S 2019 *Adv. Mater.* **31** 1900428
[8] Lin S, Zhang B, Lv T Y, Zheng J C, Pan H, Chen H, Lin C, Li X and Zhou J 2021 *ACS Omega* **6** 26689
[9] Liu D, Li Q, Jing H and Wu K 2019 *RSC Adv.* **9** 3279
[10] Liu W, Huang X, Li Q, Yao Q, Zhang D, Zhou T, Li X and Chu L 2025 *Sci. China Mater.* **68** 3737
[11] Li B, Di H, Chang B, Yin R, Fu L, Zhang Y N and Yin L 2021 *Adv. Funct. Mater.* **31** 2007447
[12] Duan C, Zou F, Wen Q, Qin M, Li J, Chen C, Lu X, Ding L and Yan K 2023 *Adv. Mater.* **35** 2300503
[13] Chen M, Ju M G, Garces H F, Carl A D, Ono L K, Hawash Z, Zhang Y, Shen T, Qi Y, Grimm R L, Pacifici D, Zeng X C, Zhou Y and Padture N P 2019 *Nat. Commun.* **10** 1
[14] Ju M G, Dai J, Ma L and Zeng X C 2017 *J. Am. Chem. Soc.* **139** 8038
[15] Jiang M and Tang J 2021 *J. Opt. Soc. Am. B* **38** 3754
[16] Shum K, Chen Z, Qureshi J, Yu C, Wang J J, Pfenninger W, Vockic N, Midgley J and Kenney J T 2010 *Appl. Phys. Lett.* **96** 221903
[17] Salem M S, Shaker A, Othman M S, Al-Bagawia A H, Fedawy M and Aleid G M 2022 *Opt. Mater.* **123** 111880
[18] Sobayel K, Akhtaruzzaman M, Rahman K S, Ferdaous M T, Al-Mutairi Z A, Alharbi H F, Alharthi N H, Karim M R, Hasmady S and Amin N 2019 *Results Phys.* **12** 1097
[19] Sarkar J, Talukdar A, Debnath P and Chatterjee S 2023 *J. Comput. Electron.* **22** 1075
[20] Dubey K C, Srivastava A, Wadhwani N and Shukla R K 2025 *J. Electron. Mater.* **54** 1851
[21] Burgelman M, Nollet P and Degrave S 2000 *Thin Solid Films* **361** 527
[22] Zhou T, Huang X, Yao R, Zhang D, Liu W and Li X 2025 *Adv. Theor. Simul.* **8** 2401064
[23] Wu B, Zhou Y, Xing G, Xu Q, Garces H F, Solanki A, Goh T W, Padture N P and Sum T C 2017 *Adv. Funct. Mater.* **27** 1604818
[24] Tvingstedt K, Gil-Escrig Ln, Momblona C, Rieder P, Kiermasch D, Sessolo M, Baumann A, Bolink H J and Dyakonov V 2017 *ACS Energy Lett.* **2** 424
[25] Krishnamoorthy T, Ding H, Yan C, Leong WL, Baikie T, Zhang Z, Sherburne M, Li S, Asta M, Mathews N and Mhaisalkar S G 2015 *J. Mater. Chem. A* **3** 23829
[26] Ming W, Shi H and Du M H 2016 *J. Mater. Chem. A* **4** 13852
[27] Kumar M H, Dharani S, Leong W L, Boix P P, Prabhakar R R, Baikie T, Shi C, Ding H, Ramesh R, Asta M, Graetzel M, Mhaisalkar S G and Mathews N 2014 *Adv. Mater.* **26** 7122
[28] Johnston M B and Herz L M 2016 *Acc. Chem. Res.* **49** 146
[29] Stolterfoht M, Grischek M, Caprioglio P, Wolff C M, Gutierrez-Partida E, Pena-Camargo F, Rothhardt D, Zhang S, Raoufi M, Wolansky J, Abdi-Jalebi M, Stranks S D, Albrecht S, Kirchartz T and Neher D 2020 *Adv. Mater.* **32** 2000080
[30] Sarker S, Islam M T, Rauf A, Al Jame H, Jani M R, Ahsan S, Islam M S, Nishat S S, Shorowordi K M and Ahmed S 2021 *Sol. Energy* **225** 471
[31] Braly I L, deQuilettes D W, Pazos-Outon L M, Burke S, Ziffer M E and Ginger D S 2018 *Nat. Photonics* **12** 355
[32] Fu J, Xu Q, Han G, Wu B, Huan C A, Leek M L and Sum T C 2017 *Nat. Commun.* **8** 1300
[33] Sze S M and Ng K K 2007 *Physics of Semiconductor Devices* 3rd Ed. (New York : Wiley) Chapter 2, p. 43
[34] Huang T, Zhu R and Luo D 2024 *Chin. Phys. Lett.* **41** 098501
[35] Shen J X, Zhang X, Das S, Kioupakis E and Van de Walle C G 2018 *Adv. Energy Mater.* **8** 1801027
[36] Zheng Y, Li Y, Zhuang R, Wu X, Tian C, Sun A, Chen C, Guo Y, Hua Y, Meng K, Wu K and Chen C C 2024 *Energ. Environ. Sci.* **17** 1153
[37] Ono L K, Liu S and Qi Y 2020 *Angew. Chem. Int. Ed.* **59** 6676
[38] Hall R N 1952 *Phys. Rev.* **87** 387
[39] Zhang X, Shen J X, Wang W and Van de Walle C G 2018 *ACS Energy Lett.* **3** 2329
[40] Li B, Li J, Yang G, Wu M and Yu J 2023 *Chin. Phys. B* **32** 107801
[41] Wang X, Faizan M, Zhou K, Wang X, Fu Y and Zhang L 2024 *Chin. Phys. B* **33** 107303